NASA/TM—2018-219719 IEPC–2017–537

Hybrid-Particle-In-Cell Simulation of Backsputtered Carbon Transport in the Near-Field Plume of a Hall Thruster

Maria Choi, John T. Yim, George J. Williams, and Daniel A. Herman
Glenn Research Center, Cleveland, Ohio

James H. Gilland
Ohio Aerospace Institute, Brook Park, Ohio

February 2018

NASA STI Program . . . in Profile

Since its founding, NASA has been dedicated to the advancement of aeronautics and space science. The NASA Scientific and Technical Information (STI) Program plays a key part in helping NASA maintain this important role.

The NASA STI Program operates under the auspices of the Agency Chief Information Officer. It collects, organizes, provides for archiving, and disseminates NASA's STI. The NASA STI Program provides access to the NASA Technical Report Server—Registered (NTRS Reg) and NASA Technical Report Server—Public (NTRS) thus providing one of the largest collections of aeronautical and space science STI in the world. Results are published in both non-NASA channels and by NASA in the NASA STI Report Series, which includes the following report types:

- TECHNICAL PUBLICATION. Reports of completed research or a major significant phase of research that present the results of NASA programs and include extensive data or theoretical analysis. Includes compilations of significant scientific and technical data and information deemed to be of continuing reference value. NASA counter-part of peer-reviewed formal professional papers, but has less stringent limitations on manuscript length and extent of graphic presentations.

- TECHNICAL MEMORANDUM. Scientific and technical findings that are preliminary or of specialized interest, e.g., "quick-release" reports, working papers, and bibliographies that contain minimal annotation. Does not contain extensive analysis.

- CONTRACTOR REPORT. Scientific and technical findings by NASA-sponsored contractors and grantees.

- CONFERENCE PUBLICATION. Collected papers from scientific and technical conferences, symposia, seminars, or other meetings sponsored or co-sponsored by NASA.

- SPECIAL PUBLICATION. Scientific, technical, or historical information from NASA programs, projects, and missions, often concerned with subjects having substantial public interest.

- TECHNICAL TRANSLATION. English-language translations of foreign scientific and technical material pertinent to NASA's mission.

For more information about the NASA STI program, see the following:

- Access the NASA STI program home page at http://www.sti.nasa.gov

- E-mail your question to help@sti.nasa.gov

- Fax your question to the NASA STI Information Desk at 757-864-6500

- Telephone the NASA STI Information Desk at 757-864-9658

- Write to:
  NASA STI Program
  Mail Stop 148
  NASA Langley Research Center
  Hampton, VA 23681-2199

NASA/TM—2018-219719 IEPC–2017–537

Hybrid-Particle-In-Cell Simulation of Backsputtered Carbon Transport in the Near-Field Plume of a Hall Thruster

Maria Choi, John T. Yim, George J. Williams, and Daniel A. Herman
Glenn Research Center, Cleveland, Ohio

James H. Gilland
Ohio Aerospace Institute, Brook Park, Ohio

Prepared for the
35th International Electric Propulsion Conference
sponsored by IEPC
Atlanta, Georgia, October 8–12, 2017

National Aeronautics and
Space Administration

Glenn Research Center
Cleveland, Ohio 44135

February 2018

Acknowledgments

The authors would like to like to thank the Space Technology Mission Directorate through the Solar Electric Propulsion Technology Demonstration Mission Project for funding the joint NASA GRC and JPL development of the Advanced Electric Propulsion System. The authors also would like to thank Alejandro Lopez Ortega at JPL for providing Hall2De simulation.

This report contains preliminary findings, subject to revision as analysis proceeds.

Level of Review: This material has been technically reviewed by technical management.

Available from

NASA STI Program
Mail Stop 148
NASA Langley Research Center
Hampton, VA 23681-2199

National Technical Information Service
5285 Port Royal Road
Springfield, VA 22161
703-605-6000

This report is available in electronic form at http://www.sti.nasa.gov/ and http://ntrs.nasa.gov/

Hybrid-Particle-In-Cell Simulation of Backsputtered Carbon Transport in the Near-Field Plume of a Hall Thruster

Maria Choi, John T. Yim, George J. Williams, and Daniel A. Herman
National Aeronautics and Space Administration
Glenn Research Center
Cleveland, Ohio 44135

James H. Gilland
Ohio Aerospace Institute
Brook Park, Ohio 44142

Summary

Magnetic shielding has eliminated boron nitride (BN) erosion as the life-limiting mechanism in a Hall thruster but has resulted in erosion of the front magnetic field pole pieces. Recent experiments show that the erosion of the graphite pole covers, which are added to protect the magnetic field pole pieces, causes carbon to redeposit on other surfaces, such as the BN discharge channel and cathode keeper surfaces. As a part of the risk-reduction activities for Advanced Electric Propulsion System (AEPS) thruster development, this study models the transport of backsputtered carbon from the graphite front pole covers and vacuum facility walls. Fluxes, energy distributions, and redeposition rates of backsputtered carbon on the anode, discharge channel, and graphite cathode keeper surfaces are predicted.

Introduction

High-power solar electric propulsion (SEP) has been identified as a critical part of an affordable, beyond low-Earth orbit crewed-exploration architecture for NASA due to its substantially higher specific impulse than conventional chemical propulsion systems. Studies performed for NASA's Human Exploration and Operations Mission Directorate (HEOMD) and Science Mission Directorate have demonstrated that a 40-kW-class SEP capability can contribute to both near-term and future architectures and science missions (Ref. 1). Since 2012, NASA has been developing a 14-kW Hall thruster electric propulsion (EP) string that can serve as the building block for realizing a 40-kW-class SEP capability. NASA continues to evolve a human exploration approach to expand human presence beyond low Earth orbit and to do so, where practical, in a manner involving international, academic, and industry partners (Ref. 2). NASA publicly presented a phased exploration concept at the HEOMD Committee of the NASA Advisory Council meeting on March 28, 2017 (Ref. 3). NASA presented an evolutionary human exploration architecture, depicted in Figure 1, to expand human presence deeper into the solar system through a phased approach, including cislunar flight testing and validation of exploration capability before crewed missions beyond the Earth-Moon system and eventual crewed Mars missions. One of the key objectives is to achieve human exploration of Mars and beyond through the prioritization of those technologies and capabilities best suited for such a mission in accordance with the stepping stone approach to exploration (Ref. 4). High-power SEP is one of those key technologies that has been prioritized because of its significant exploration benefits. A high-power, 40-kW-class Hall thruster propulsion system provides significant capability and represents, along with flexible blanket solar array technology, a readily scalable technology with a clear path to much higher power systems.

The 14-kW Hall thruster system development, led by the NASA Glenn Research Center and the Jet Propulsion Laboratory (JPL), began with maturation of the high-power Hall thruster and power processing unit. The technology development work has transitioned to Aerojet Rocketdyne via a competitive procurement selection for the Advanced Electric Propulsion System (AEPS). The AEPS contract includes the development, qualification, and multiple flight 14-kW EP string deliveries. The

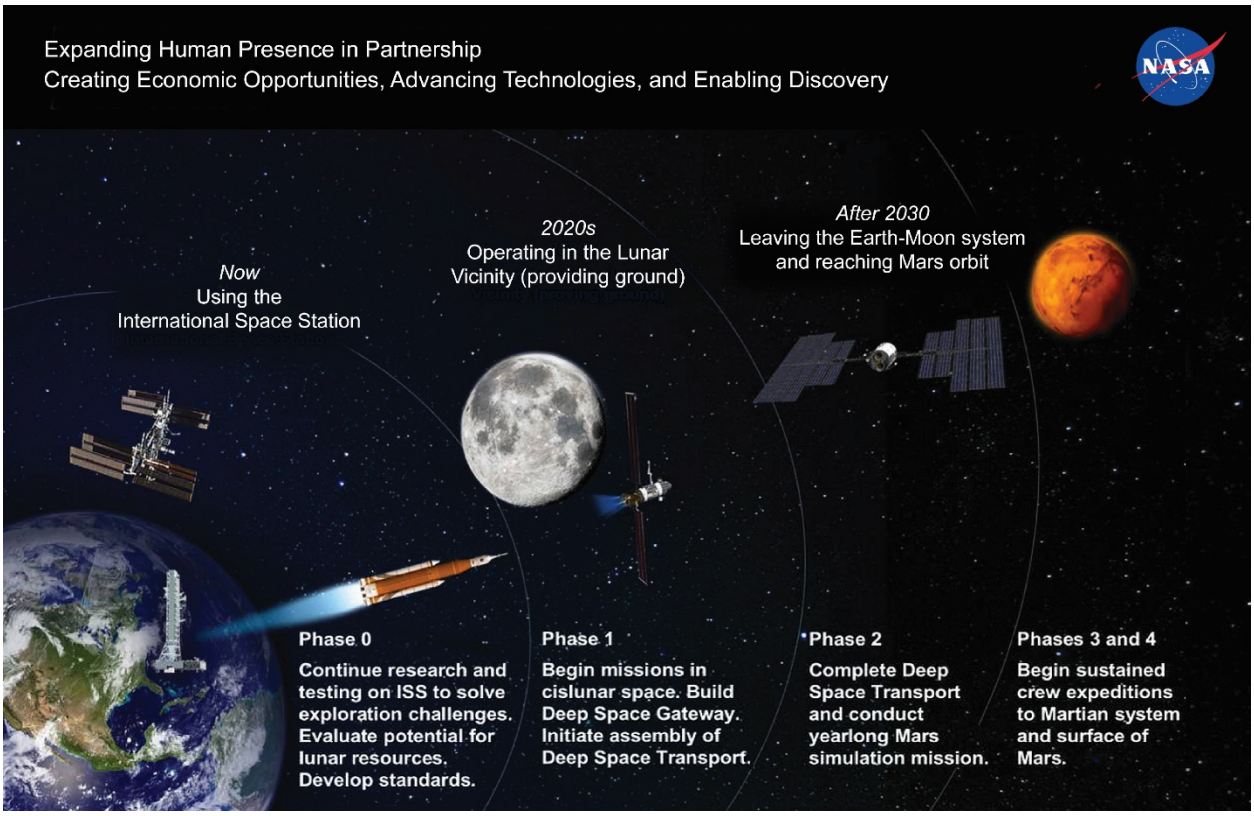

Figure 1.—NASA Human Exploration Vision including Deep Space Gateway and Deep Space Transport (Ref. 4). ISS, International Space Station.

AEPS EP string consists of the Hall thruster, power processing unit (including digital control and interface functionality), xenon (Xe) flow controller, and associated intra-string harnesses. NASA continues to support the AEPS development by leveraging in-house expertise, plasma modeling capability, and world-class test facilities. NASA also executes AEPS and mission risk reduction activities to support AEPS development and mission application. An overview of the NASA and Aerojet development activities and mission application of the AEPS Hall thruster system is provided by Herman (Ref. 5).

While the lifetime of conventional Hall thrusters has been limited by the erosion of discharge channel walls, magnetic shielding in Hall thrusters (Refs. 6 and 7) eliminated the discharge channel wall erosion as the primary failure mechanism of Hall thrusters. However, previous wear testing of magnetically shielded Hall thrusters showed that the erosion of other surfaces was increased (Refs. 8 to 11). While the reduction in the discharge channel wall erosion in magnetically shielded Hall thrusters surpasses the relatively slow increase in erosion rates in the front poles (Ref. 11), the erosion on the inner magnetic pole piece surface now constitutes the primary erosion-based service life-limiting mechanism. To reduce the risk of the magnetic circuit being eroded, the thruster design was updated to include front pole covers made of graphite—an erosion-resistant material. Despite the employment of erosion-resistant material, Xe-ion bombardment on the graphite pole covers resulted in backsputtered carbon, and the rate at which carbon sputters from the inner front pole cover (IFPC) is now greater than the vacuum facility backsputter rate. Redeposition of these carbon particles has been observed on various parts of the thruster, including the anode, boron nitride (BN) discharge channel walls, and cathode keeper surfaces (Ref. 12). While the carbon population is still too low to affect thruster performance, it could affect how much carbon is getting to the thruster surfaces, which is important for proper erosion determination and thruster lifetime assessment.

Since a detailed understanding of the ionization and redeposition rates of backsputtered carbon is of great value added to the risk-reduction activities for Hall Effect Rocket with Magnetic Shielding (HERMeS) thruster development, the present study simulates transport of backsputtered carbon from both the vacuum facility walls and graphite front pole covers of the thruster. In this paper, transport of carbon in the near-field plume and the inside discharge channel is modeled using the direct simulation Monte Carlo (DSMC) combined with the particle-in-cell (PIC) method. Backsputter rates from the vacuum facility walls and the regression rates of the front pole covers are measured and fed into the model as an input. Fluxes, energy distributions, and redeposition rates of carbon on various surfaces are predicted.

The erosion and performance characterization of HERMeS observed in short-duration tests is discussed in companion papers, References 12 and 13, respectively. Other risk-reduction activities are currently ongoing at Glenn and JPL, including surface layer activated wear testing (Ref. 14), extensive numerical modeling (Ref. 15), assessment of the impact of carbon deposition on service-life assessment (Ref. 16), and laser-based characterization of near-field ions (Ref. 17).

Nomenclature

AEPS	Advanced Electric Propulsion System
BN	boron nitride
BOL	beginning of life
CEX	charge exchange
DSMC	Direct Simulation Monte Carlo
EP	Electric Propulsion
HAP	Hypersonic Aerothermodynamics Particle
HEOMD	Human Exploration and Operations Mission Directorate
HERMeS	Hall Effect Rocket with Magnetic Shielding
HV	high voltage
IC	inner channel
IFPC	inner front pole cover
ISS	International Space Station
JPL	Jet Propulsion Laboratory
MEX	momentum exchange
OC	outer channel
OFPC	outer front pole cover
PIC	particle-in-cell
QCM	quartz crystal microbalance
SEP	solar electric propulsion
TDU–1	Technology Demonstration Unit 1
VDF	velocity distribution function
VF–5	Vacuum Facility 5
VHS	variable hard sphere

A	fitting coefficient (as defined in Table 2)
B	fitting coefficient (as defined in Table 2)
C	fitting coefficient (as defined in Table 2)
D	fitting coefficient (as defined in Table 2)
E	energy
E_i	ionization potential
f_E	Sigmund-Thompson energy distribution
g	colliding particles
m	interatomic potential exponent parameter
N	local number density
p	collision pair value
q	collision pair value
T_e	electron temperature
U_b	binding energy
α	fitting coefficient (as defined in Table 2)
σ	total cross section
Δt	time step size

Carbon Transport Modeling Description

Numerical Model

The transport of backsputtered carbon is simulated using the two-dimensional axi-symmetric DSMC-PIC code developed by the University of Michigan (Ref. 18). Since carbon (C) densities are several orders of magnitude smaller than Xe densities (as shown in Figure 2), carbon will not have a significant impact on plasma properties or thruster performance. Therefore, a time-averaged plasma simulation solution from JPL-developed Hall2De (Ref. 15) is used to provide a fixed Xe plasma background flow. The electron temperature, electric fields, and the number densities and velocities of Xe plasma and electrons are interpolated to the computational mesh and are fixed constant in time. The current Hall2De solution contains three fluids for three Xe ion species: Xe^{+}, Xe^{2+}, and Xe^{3+}, totaling nine Xe ion species (Ref. 15). The present study simulates atomic carbon neutrals (C) and ions (C^{+}) and does not include carbon clusters (e.g., C_2 and C_3), even though they may be important in backsputtering calculations (Refs. 19 and 20).

In this study, two basic classes of important collision mechanisms in Hall thrusters are implemented: the momentum exchange (MEX) and charge exchange (CEX) collisions. Table 1 summarizes the detailed collision classes modeled in this study. The collisions between C–C and C–C+ are neglected due to their low densities (Figure 2).

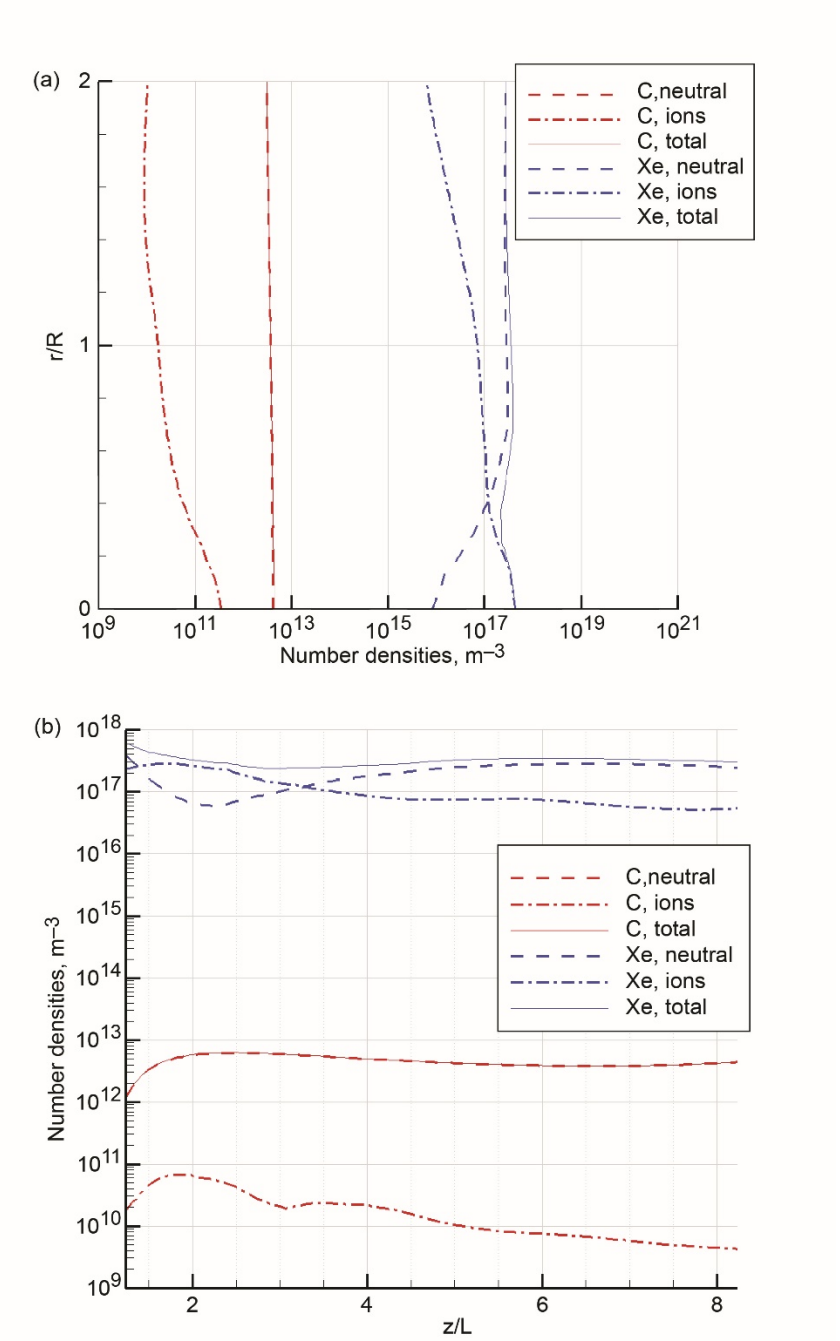

Figure 2.—Comparisons of number densities of Xe versus carbon extracted. (a) In radial direction just downstream of front pole cover exit plane. (b) In axial direction along channel centerline. Both plots show that total carbon density is approximately five orders of magnitude lower than total Xe number densities.

TABLE 1.—COLLISION CLASSES MODELED IN THIS STUDY

	Xe	Xe^+	Xe^{2+}	Xe^{3+}	C	C^+
C	MEX[a]	MEX, CEX[b]	MEX	MEX	none	none
C^+	MEX, CEX	MEX	MEX	MEX	none	none

[a]Momentum exchange.
[b]Charge exchange.

A list of colliding particle pairs in each cell are selected at random, regardless of their relative positions and velocities, to perform binary collisions. The collision probability of each pair is calculated at each time step, and is proportional to the product of the relative velocity between the colliding particles, g, and the total cross section, σ. In each cell, the number of ionized particles and the total number of possible collision candidate pairs for each time step is calculated using Bird's No-Time-Counter (Ref. 21). For a collision pair, p and q, the number of collisions that can occur is

$$N_{pq} = \frac{1}{2} N_p N_q (\sigma g)_{pq,\max} \Delta t \tag{1}$$

where N is the local number density and Δt is the time step size. For all collision cross sections, the variable hard sphere (VHS) (Ref. 22) model is employed. Once the collision probability is calculated, it is compared with a random number to determine whether a collision occurs or not. If a collision occurs, the post-collision velocities are calculated using conservation of momentum and energy and assuming isotropic scattering. Only the C and C^+ species properties are updated.

The model also includes the electron-impact ionization of carbon neutrals. For the ionization cross section, this study uses modified Younger's formula (Ref. 21)

$$\sigma_{i,(c)} = \frac{\alpha}{\left(u + \frac{E_i}{\pi}\right) E_i^2} \left[A\left(1 - \frac{1}{u}\right) + B\left(1 - \frac{1}{u}\right)^2 + C\ln(u) + \frac{D}{u}\ln(u) \right] \tag{2}$$

where $u = T_e / E_i$, and T_e is the electron temperature, E_i is the ionization potential, and α and A to D are the fitting coefficients to fit Brook's ionization data (Ref. 22), as defined in Table 2. The resulting ionization cross-section curve is shown in Figure 3.

TABLE 2.—PARAMETERS USED IN THIS STUDY FOR EQUATION (2) TO FIT BROOK'S ELECTRON IMPACT IONIZATION DATA (REF. 24) FOR CARBON

α	E_i, eV	A	B	C	D
360.0	11.26	12.2	–3.91	1.85	–10.3

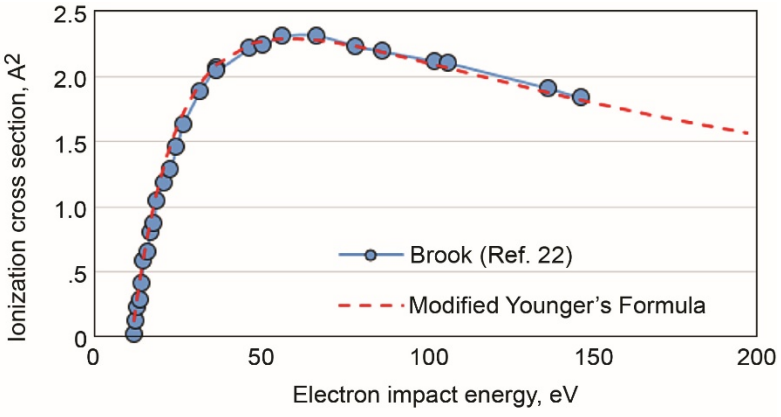

Figure 3.—Electron impact ionization cross section for carbon atom.

Computation Domain and Boundary Conditions

The computation domain is shown and labeled in Figure 4, which includes near-field plume and discharge channel regions. The domain consists of 3,500 cells, and about 0.9 million carbon macroparticles are used. Carbon neutrals are introduced from the IFPC, the outer front pole cover (OFPC), and the axial and radial far-field boundaries. No flow is introduced from the anode or the cathode, as plasma properties from a Hall2De solution are fixed in the background.

The fluxes of carbon backsputtered from front pole covers are based on the Technology Demonstration Unit 1 (TD–1) wear test measurement (Ref. 10). During the short-duration wear test of TDU-1 in Vacuum Facility 5 (VF–5) at the nominal 600-V, 12.5-kW operating condition, the net erosion rates of the IFPC were approximately 25.0 μm/khr, and no measurable erosion and/or deposition was measured from the OFPC. The fluxes of carbon backsputtered from the VF—5 chamber walls are based on the quartz crystal microbalance (QCM) data (Ref. 16). The mean backsputter rate in the axial direction measured by QCM for this test was approximately 1.8 μm/khr, and the radial direction is assumed to be about 20 percent of the axial rate, based on our recent measurement. Assuming that all facility backsputter carbon particles stick to the graphite front pole covers during this operation, the fluxes of carbon atoms introduced in the computation domain are summarized in Table 3. Although the axial far-field boundary is not at the QCM location, the backsputter rate at the far-field boundary is assumed to be equivalent to the rate at the QCM location, which is at the thruster exit plane. The chamber backpressure during this operation was approximately 4.6×10^{-6} torr, corrected for Xe.

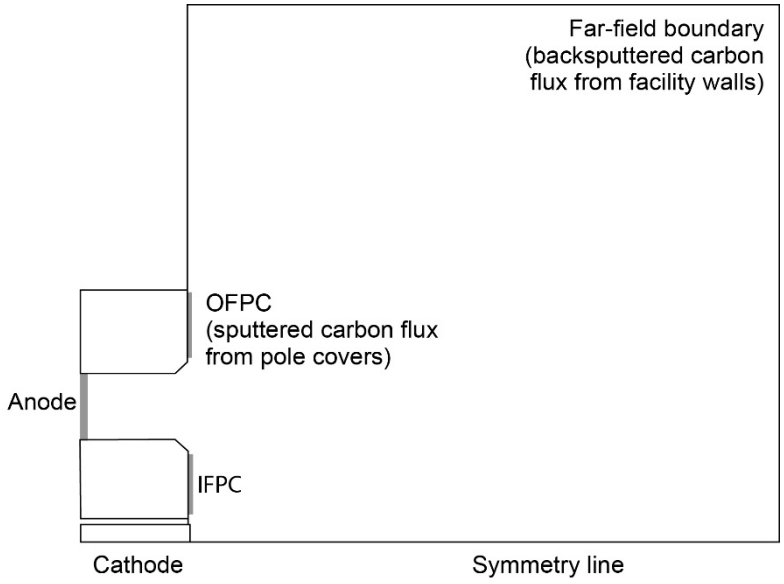

Figure 4.—Two-dimensional axisymmetric computational domain and labels on each boundary (not drawn to scale). Carbon atoms are introduced on inner front pole cover (IFPC) and outer front pole cover (OFPC) as well as far-field boundaries (top and right).

TABLE 3.—NUMBER FLUXES ($M^{-2}S^{-1}$) OF CARBON ATOMS AT EACH INFLOW BOUNDARY

IFPC[a]	OFPC[b]	Axial far-field	Radial far-field
8.4×10^{17}	5.7×10^{16}	5.7×10^{16}	1.1×10^{16}

[a]Inner front pole cover.
[b]Outer front pole cover.

The energy, E, of sputtered particles from a surface is characterized using the well-known Sigmund-Thompson energy distribution (Ref. 25)

$$f_E \propto \frac{E}{\left(E + U_b^2\right)^{3-2m}} \tag{3}$$

where $U_b = 7.4$ eV is the binding energy, and m = 1/3 is the interatomic potential exponent parameter. This distribution normalized by its area is shown in Figure 5, and has the most probable energy of 5.6 eV. In order to simplify the modeling process, particles are sampled using the Maxwellian velocity distribution functions (VDFs) with the same most probable energy as a first approximation (shown by the blue dashed curve in Figure 5). By matching the most probable energies of both distributions, the spread in the Maxwellian distribution is much narrower and the peak is about 2.5 times higher than the Sigmund-Thompson distribution. This means that, by making the assumption of Maxwellian VDF, we are underestimating carbon atoms with higher energies and overestimating carbon atoms with lower energies. However, this underestimation and overestimation of higher and lower energy carbon atoms, respectively, has a negligible effect on the total collision cross sections, since carbon energy is very low compared to beam ion energy.

In classical theory, the angular distribution of sputtered particles follows cosine distribution, as shown by the blue curve of the polar plot (Figure 6(a)). Experimental measurements of differential sputter yields show that particles are sputtered following an under-cosine profile (Refs. 19 to 26), such as that of Figure 6(b). The angular distribution of sputtered particles becomes more cosine-like when the incidence energy is lower (Ref. 26). The expected energy range of incident Xe ions is in the low ranges (< 100 eV) for the IFPC (Ref. 12), which makes the cosine distribution a reasonable assumption for a first approximation. Alternately, because the far-field boundary of the simulation is still far away from the actual vacuum chamber walls, uniform angular distribution is assumed, as shown by the red curve in Figure 6(b).

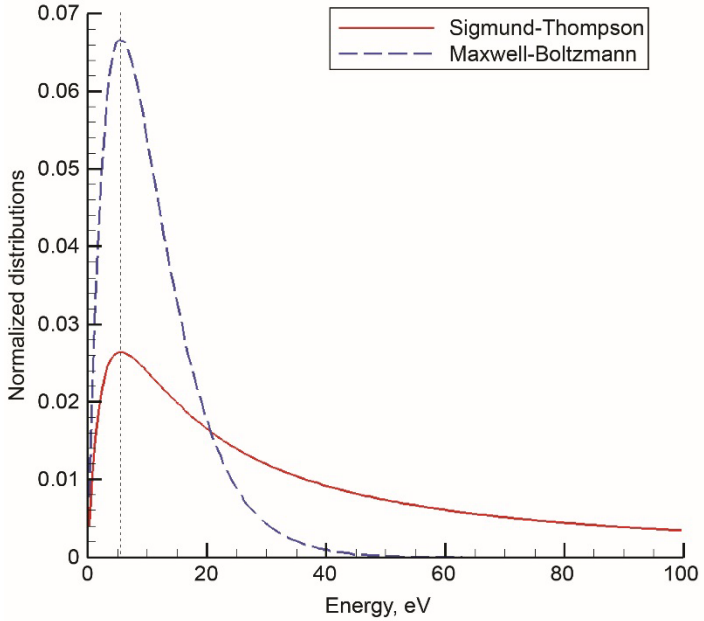

Figure 5.—Comparison of Sigmund-Thompson distribution (red) and sampled energy distribution for backsputtered carbon, assuming Maxwellian velocity distribution function (VDF) (blue). By matching most probable energy of 5.6 eV, carbon with higher and lower energies is underestimated and overestimated, respectively.

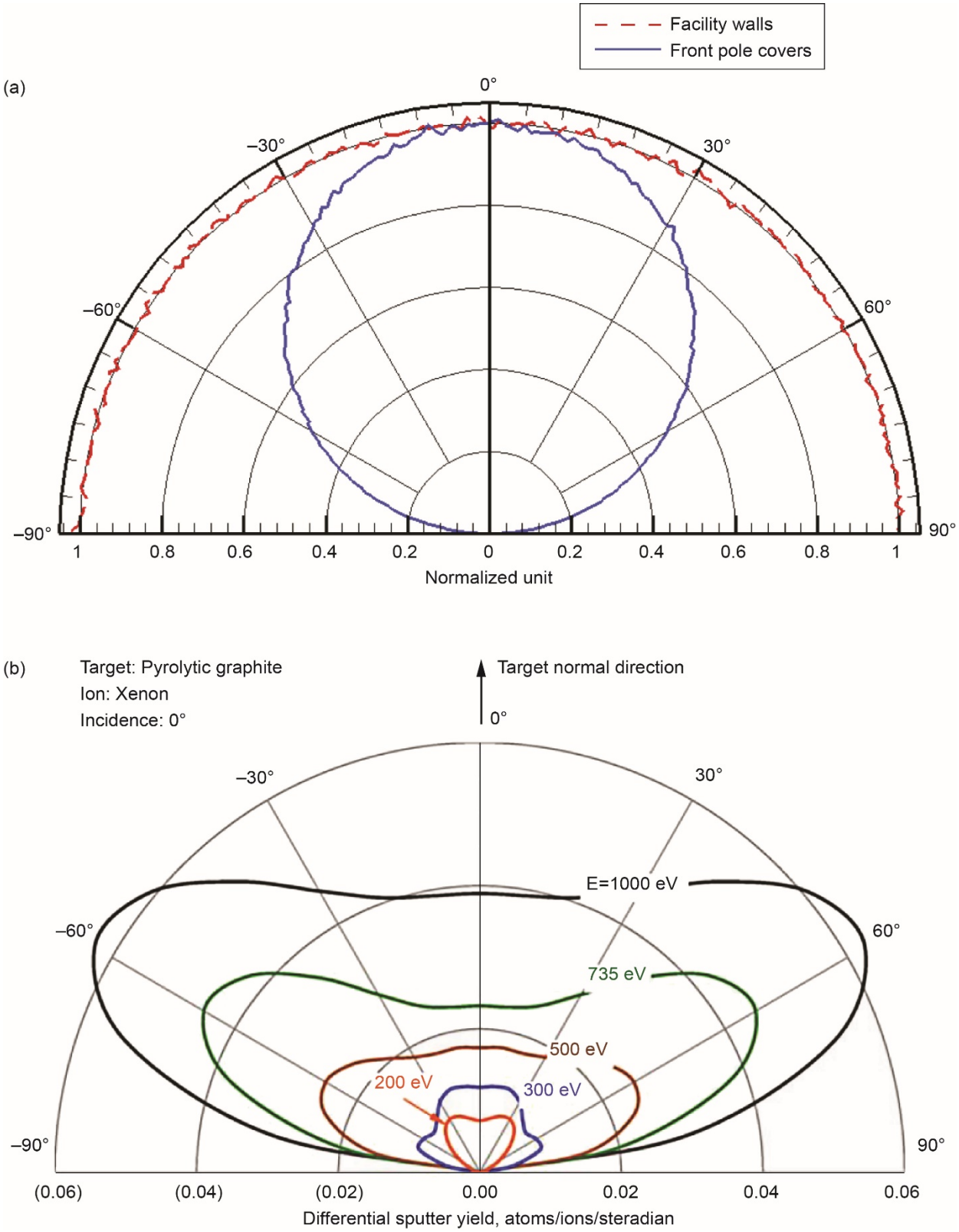

Figure 6.—Polar plots of angular distributions. (a) Sampled carbon atoms at inner front pole cover (IFPC) in simulation. (b) Measurement from Reference 26.

When carbon particles hit surfaces, they are assumed to reflect diffusely. The temperature of all surfaces is assumed to be 900 K. The sticking coefficients for the anode, the BN discharge channel, and the graphite cathode keeper are 0.65, 0.99, and 0.99, respectively. Once a carbon coating is formed, the sticking will be the same as for a carbon surface. Therefore, since this study is concerned with a wear test, the sticking coefficient of 0.99 is used also for the anode surface. Lastly, no carbon clusters (e.g., C_2 and C_3) are modeled for the present work, even though they may be important in backsputtering calculations (Refs. 19 and 20).

Results and Discussions

In this section, steady-state results of carbon transport simulation are presented. The backsputtered carbon species from the facility walls and the IFPC and OFPC are separately tracked in the model to quantify redeposition amounts of species on various surfaces.

Simulation Results

Figure 7(a) shows the generation of carbon ion particles, and the legend represents the number of macro ions generated during the simulation. The purpose of this plot is to indicate the locations of where carbon atoms get ionized, which are in the acceleration and ionization region and downstream of the cathode plume region. Recalling Equations (1) and (2), the carbon ion generation in these regions corresponds to the regions of high electron temperature and electron number densities. Figure 7(b) to (d) show the time-averaged Hall2De solution of electron temperature, number density, and plasma potential, respectively, interpolated on the computational grid used in this study for the 600 V, 12.5-kW nominal condition.

The carbon neutral and ion number densities are plotted in Figure 8(a) and Figure 9(a), respectively. The carbon neutral density ranges from 2.8×10^{11} to 4.4×10^{13} m^{-3} in the computational domain, while carbon ion density ranges from 1×10^{5} (minimum density) to 1.7×10^{12} m^{-3}. Figure 8(b) to (d) show the number densities of carbon neutrals from the IFPC, the OFPC, and facility walls, respectively. When carbon atoms are generated at these inflow boundaries, they move with their initial velocities until they undergo collisions with the background Xe species, whether they are Xe neutrals or ions. Carbon-neutral densities from both the IFPC and OFPC decrease away from the pole surfaces monotonically with spherical shape. The facility backsputter carbon density also decreases monotonically from the top and right far-field boundaries due to collisions with the plasma. In the previous backsputter carbon modeling effort (Ref. 16), nonuniform carbon fluxes in the vacuum chamber were predicted using the Hypersonic Aerothermodynamics Particle (HAP) code (Ref. 27). Still, the decrease in the carbon number density predicted in this study is higher than expected. While some of this reduction in the density may be physical, sensitivity studies are currently underway to examine whether this is a result of isotropic assumption and small domain.

When these backsputtered carbon neutrals collide with electrons, mostly in the acceleration and ionization region by the channel as seen in Figure 7(a), they are ionized. Then, carbon ions are accelerated in the direction of electric field, calculated by the negative gradient of the plasma potential from Figure 7(d). In Figure 9, the number densities of the IFPC, the OFPC, and facility carbon ions are plotted. Some of the ions born in the acceleration and ionization region are accelerated downstream, following the axial electric field, and some follow the radial potential drop towards the cathode, resulting in the highest carbon ion densities along the cathode centerline, as shown in Figure 9. The carbon ions generated downstream of the cathode plume also migrate upstream toward the cathode, following the axial electric field pointing toward the cathode.

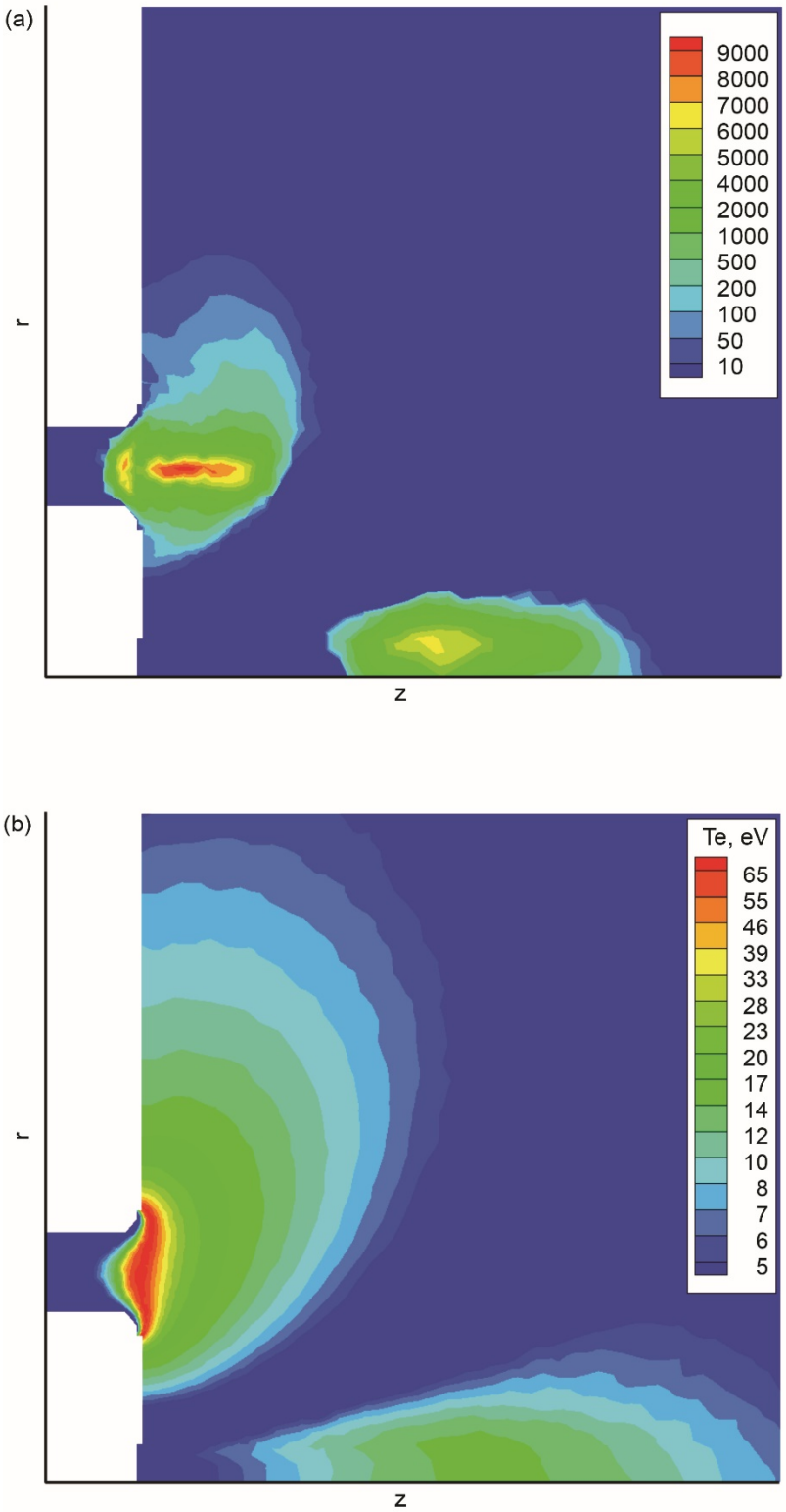

Figure 7.—Contour plots. (a) Generation of carbon ions calculated from the DSMC-PIC code. (b) Electron temperature, (c) electron number density, (d) plasma potential, as calculated by Hall2De.

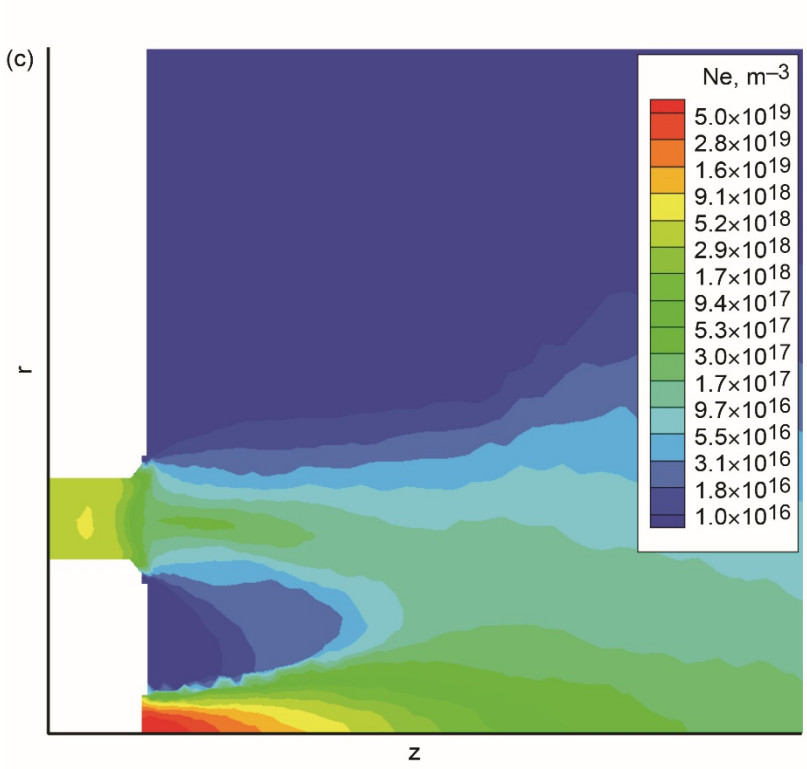

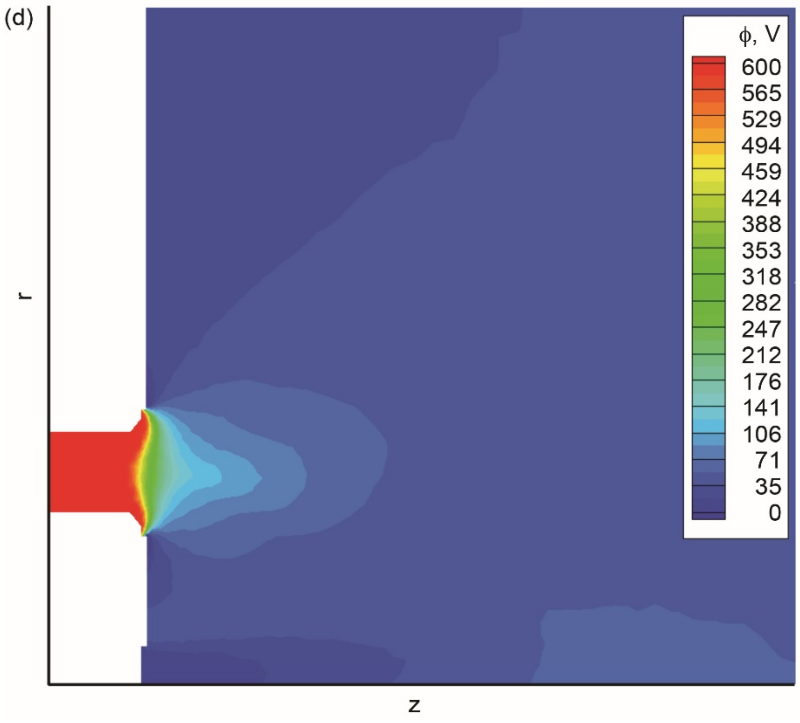

Figure 7.—Concluded.

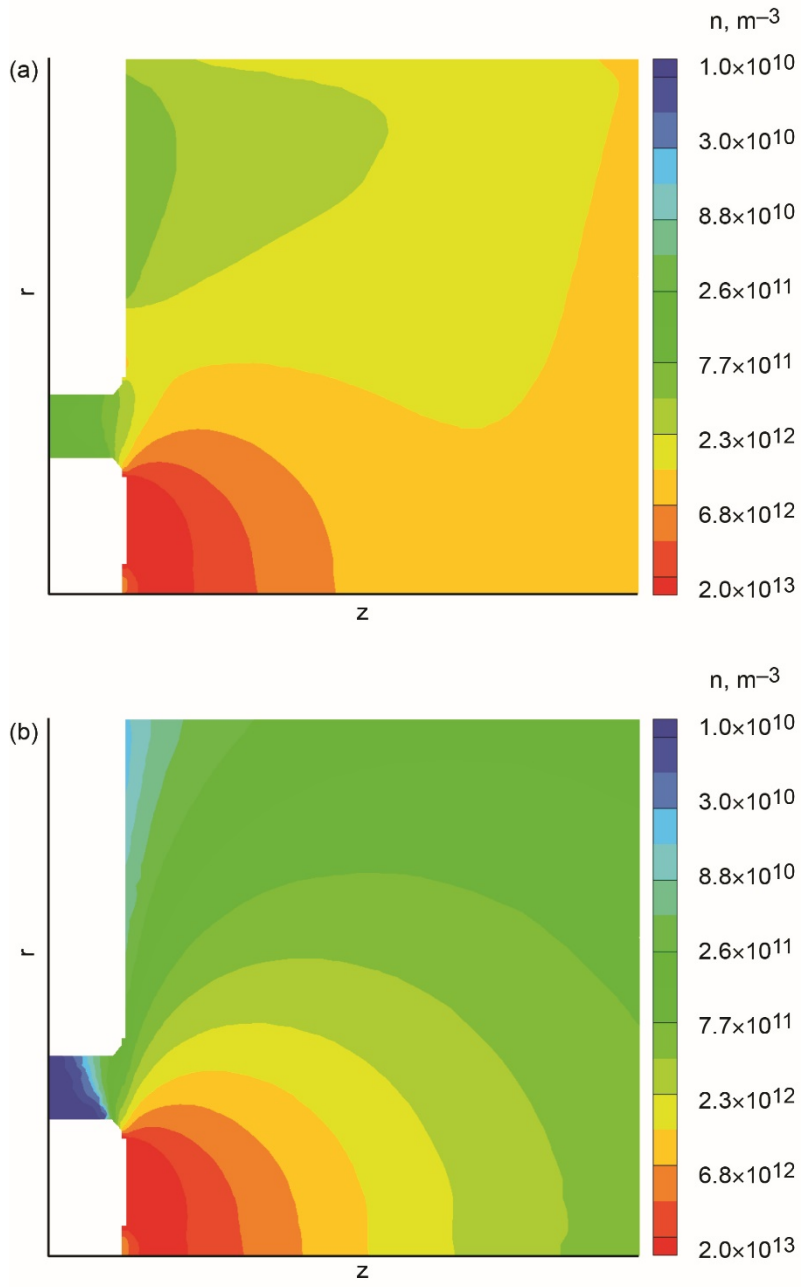

Figure 8.—Number densities. (a) Total carbon atoms. (b) Inner front pole cover (IFPC) carbon atoms. (c) Outer front pole cover (OFPC) carbon atoms. (d) Facility backsputter carbon atoms.

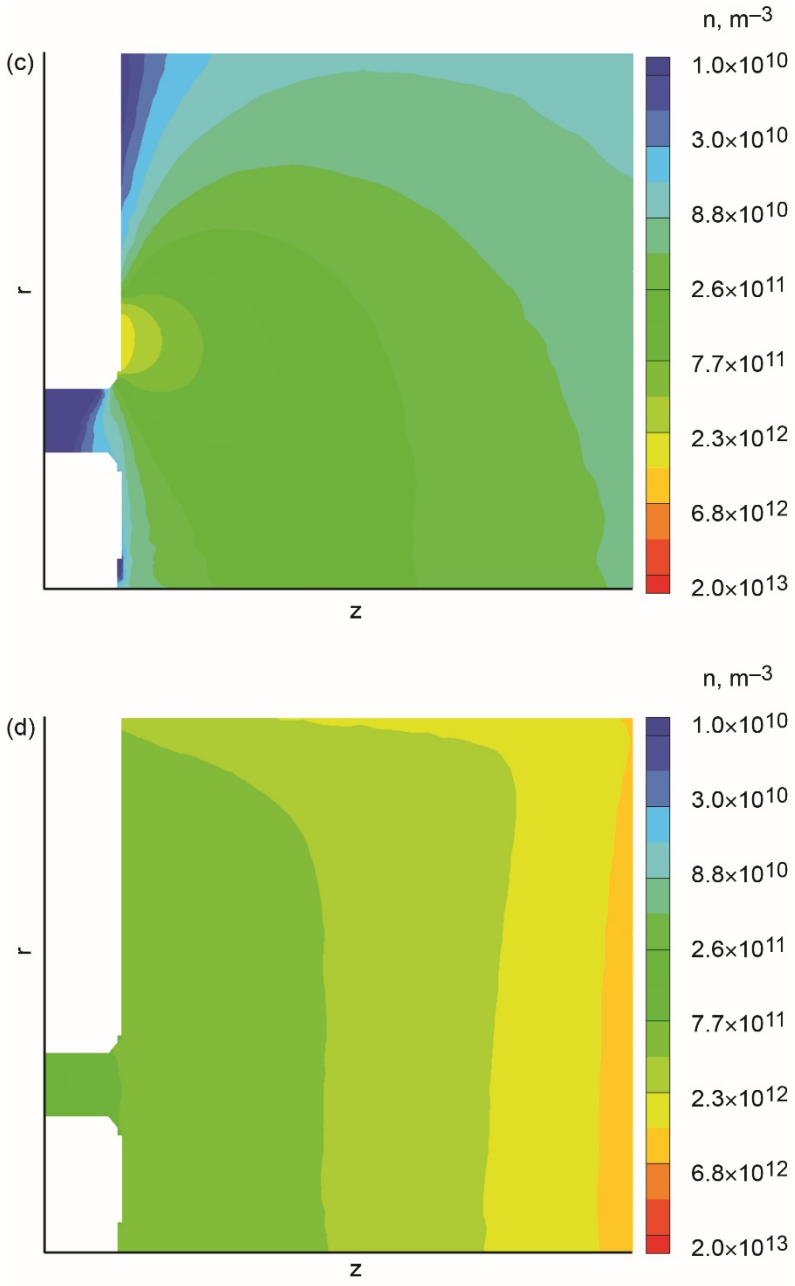

Figure 8.—Concluded.

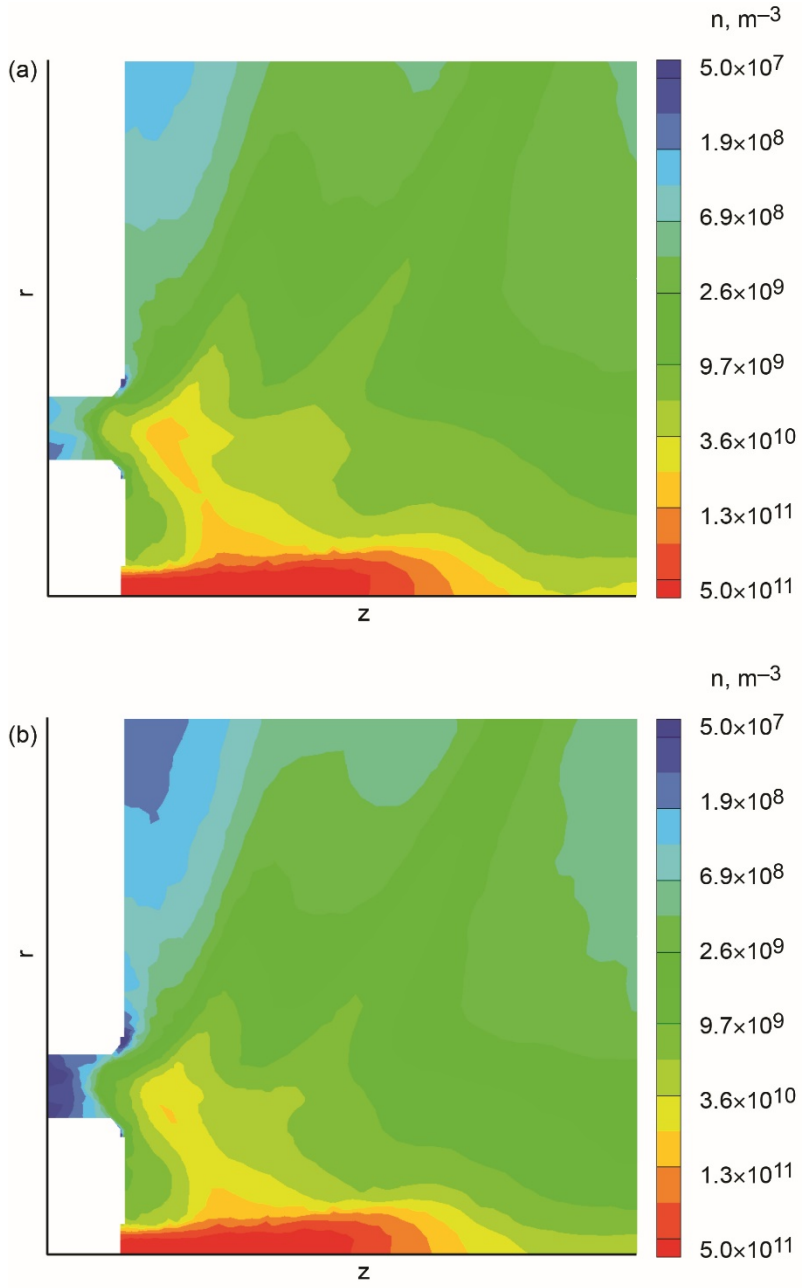

Figure 9.—Number densities. (a) Total carbon ions. (b) Inner front pole cover (IFPC) carbon ions. (c) Outer front pole cover (OFPC) carbon atoms. (d) Facility backsputter carbon ions.

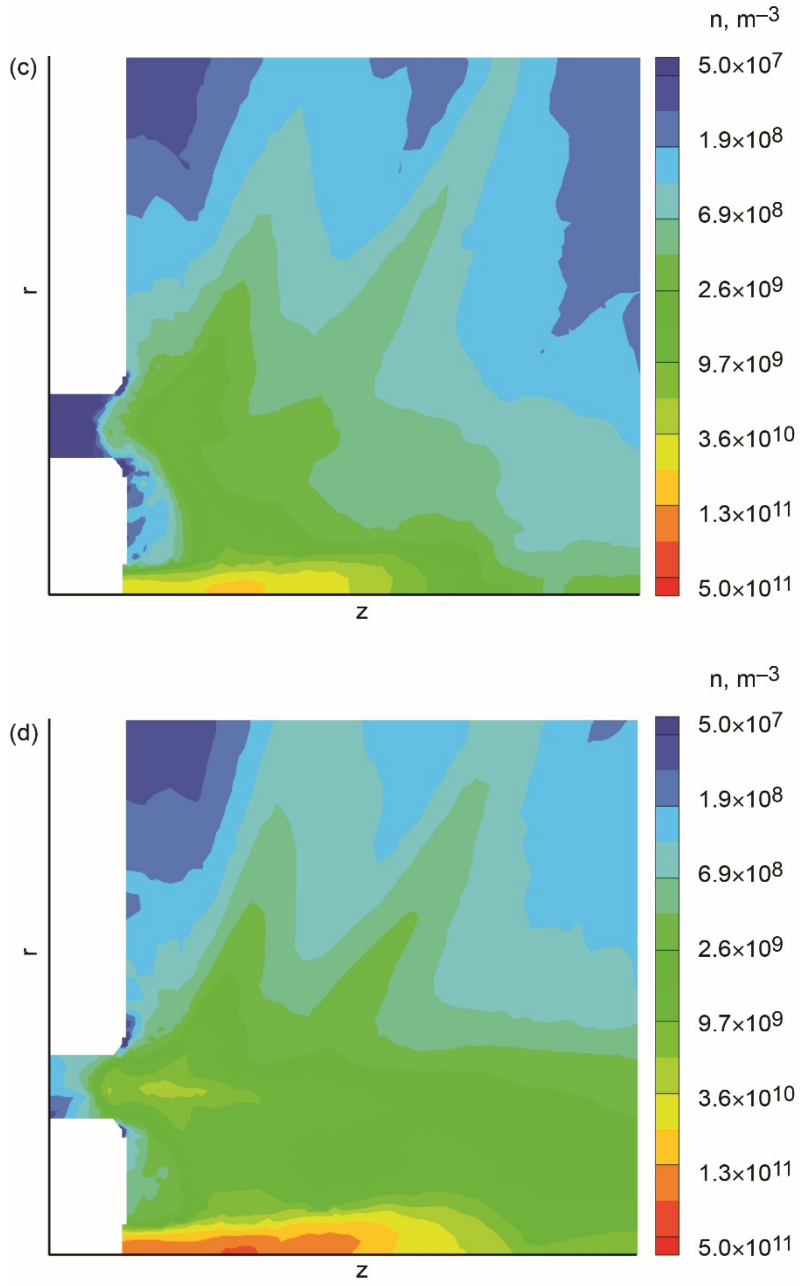

Figure 9.—Concluded.

Figure 10 shows the fluxes of backsputtered carbon arriving on the BN inner and outer discharge channel surfaces. The discharge channel wall is divided into three parts for closer examination, which are the main channel wall, chamfer, and front flat parts as shown in Figure 10(a). On the main channel wall and the chamfer of the inner channel (IC), the deposited carbon flux is dominated by carbon from the far-field boundaries, which represents the vacuum facility backsputter carbon neutrals. On the front flat part of the IC, the carbon flux from the IFPC surpasses the facility carbon flux. There are either no or very small amounts of carbon ions along both the IC and outer channel (OC), because ions follow the local electric field and are accelerated out of the thruster immediately after they are generated. In Figure 10(b), the anode side to the midlength of the OC wall shows a similar amount of facility backsputter carbon neutral flux as seen in the IC wall. However, from the midchannel wall to the chamfer, the carbon neutral flux from the IFPC increases to comparable magnitudes of the facility carbon neutrals. The OFPC carbon neutral flux rapidly increases on the front flat of the channel.

Figure 11 shows the fluxes of carbon redeposited on the anode and cathode surfaces. The carbon flux on the anode is dominated by facility backsputter carbon neutrals. On the front surface of the cathode keeper, large amounts of carbon neutrals and ions from the IFPC are deposited, surpassing the amount of facility backsputtered carbon. There are also large amounts of carbon ions hitting the keeper surface. These high ion fluxes can be explained by the high ion number densities (Figure 9) and negative potential gradient (Figure 7(d)) previously discussed. The energy distribution of depositing carbon particles is examined to determine its full effect on the cathode keeper.

Figure 12(a) shows the energy distributions collected on the IC, OC, cathode, and anode surfaces. For all surfaces except the cathode keeper, energy distributions are mostly preserved from the beginning-of-life (BOL) energy distributions. The highest populations are shown around 5 to 7 eV, which is their most probable energy at generation matches the Sigmund-Thompson distribution, implying that the carbon species arriving at these surfaces did not undergo collisions. For the cathode keeper surface, a higher peak around 30 to 45 eV is added to its BOL distribution. This higher energy peak is predominantly from carbon ions (Figure 12(b)). Carbon ions gain this energy by accelerating through the potential drop towards the cathode. Currently, no sputter yield data is found for carbon ions striking a graphite surface with energies of 30 to 45 eV, currently. Thus, more investigation is required to determine whether these ions would or would not cause any erosions on the graphite keeper surface.

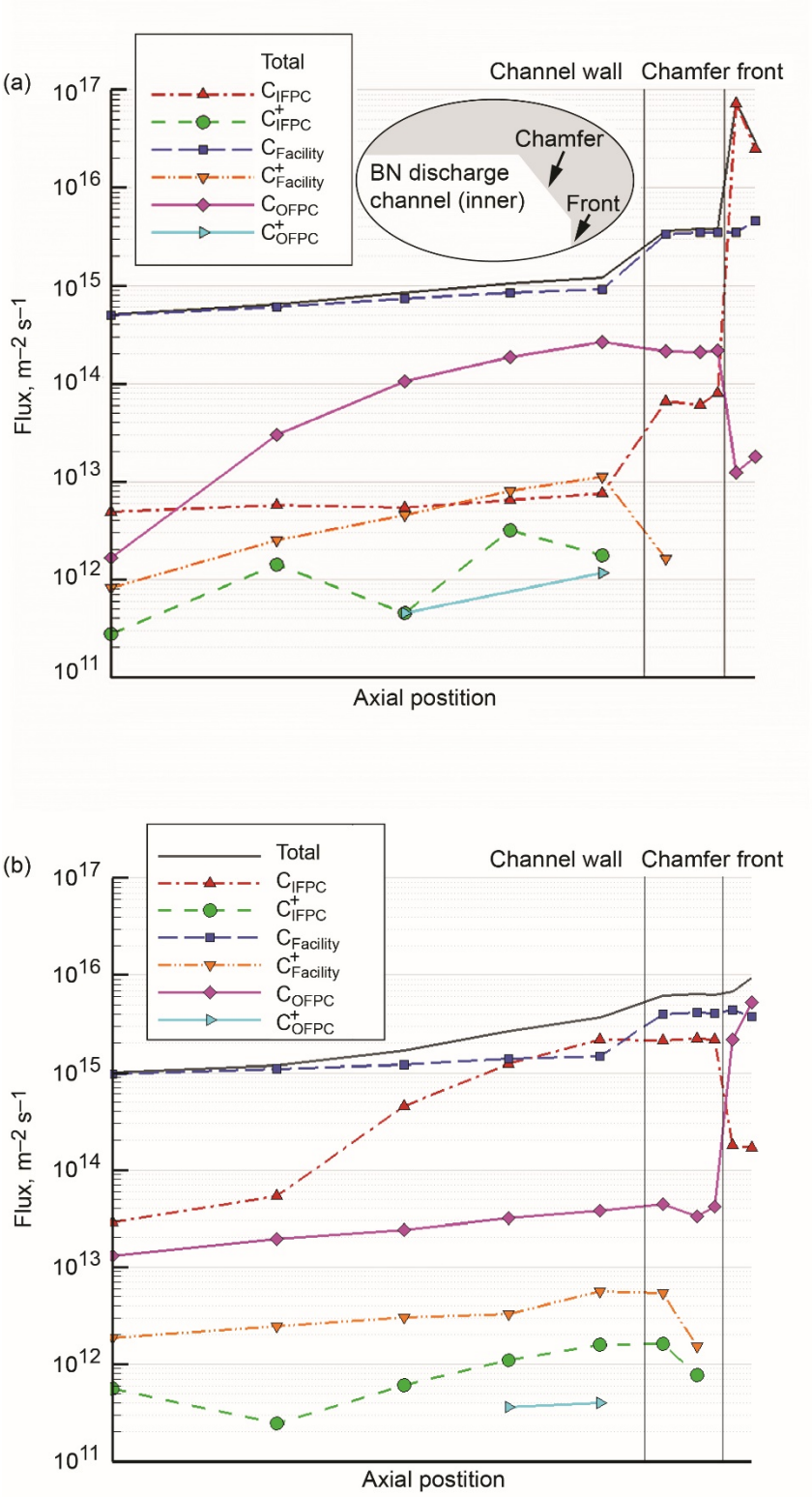

Figure 10.—Fluxes of backsputtered carbon redepositing. (a) On inner channel surface. (b) On the outer channel surface. IFPC, inner front pole cover; OFPC, outer front pole cover.

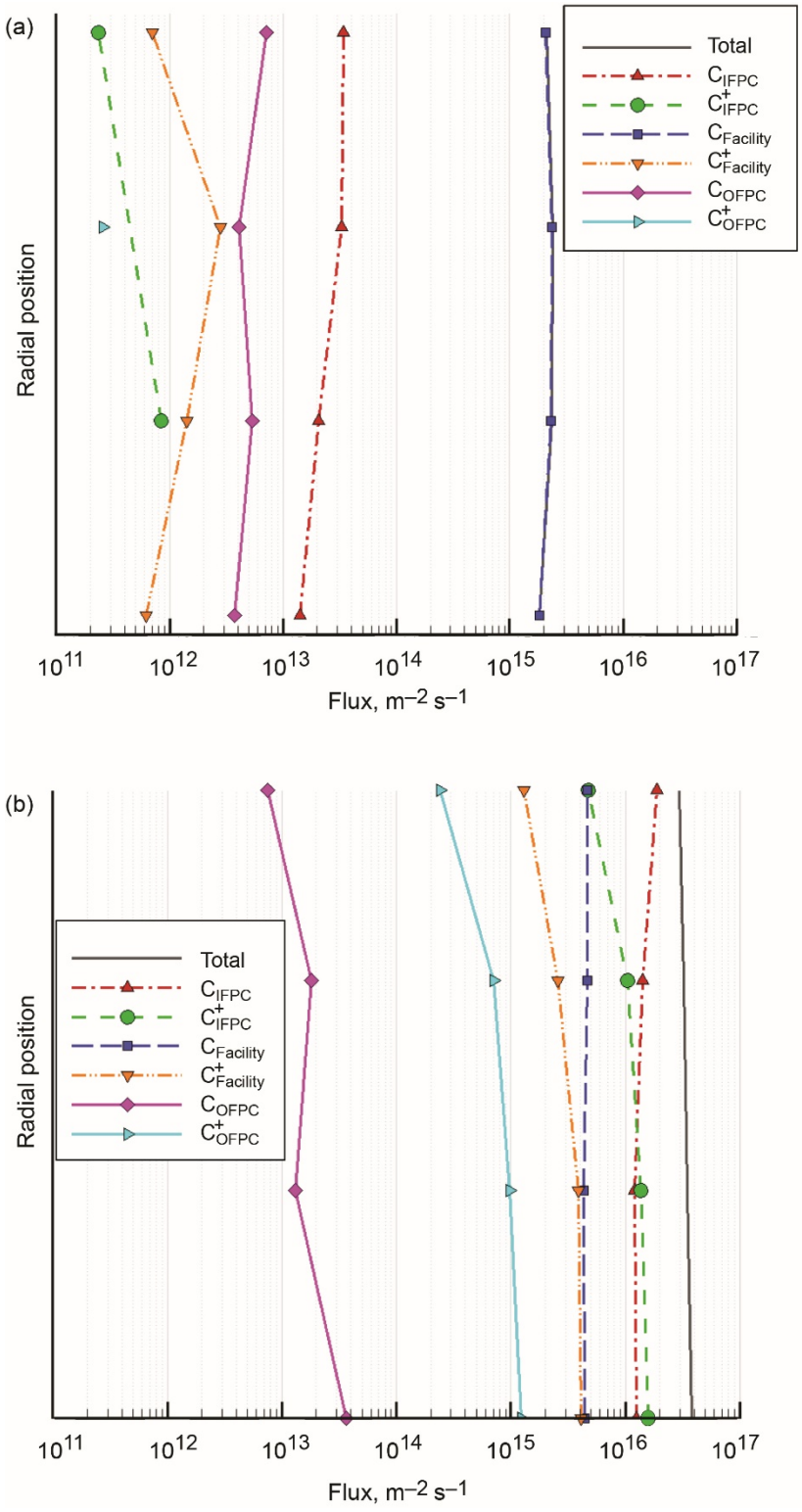

Figure 11.—Fluxes of backsputtered carbon redepositing. (a) On anode surface. (b) On the cathode surface. IFPC, inner front pole cover; OFPC, outer front pole cover.

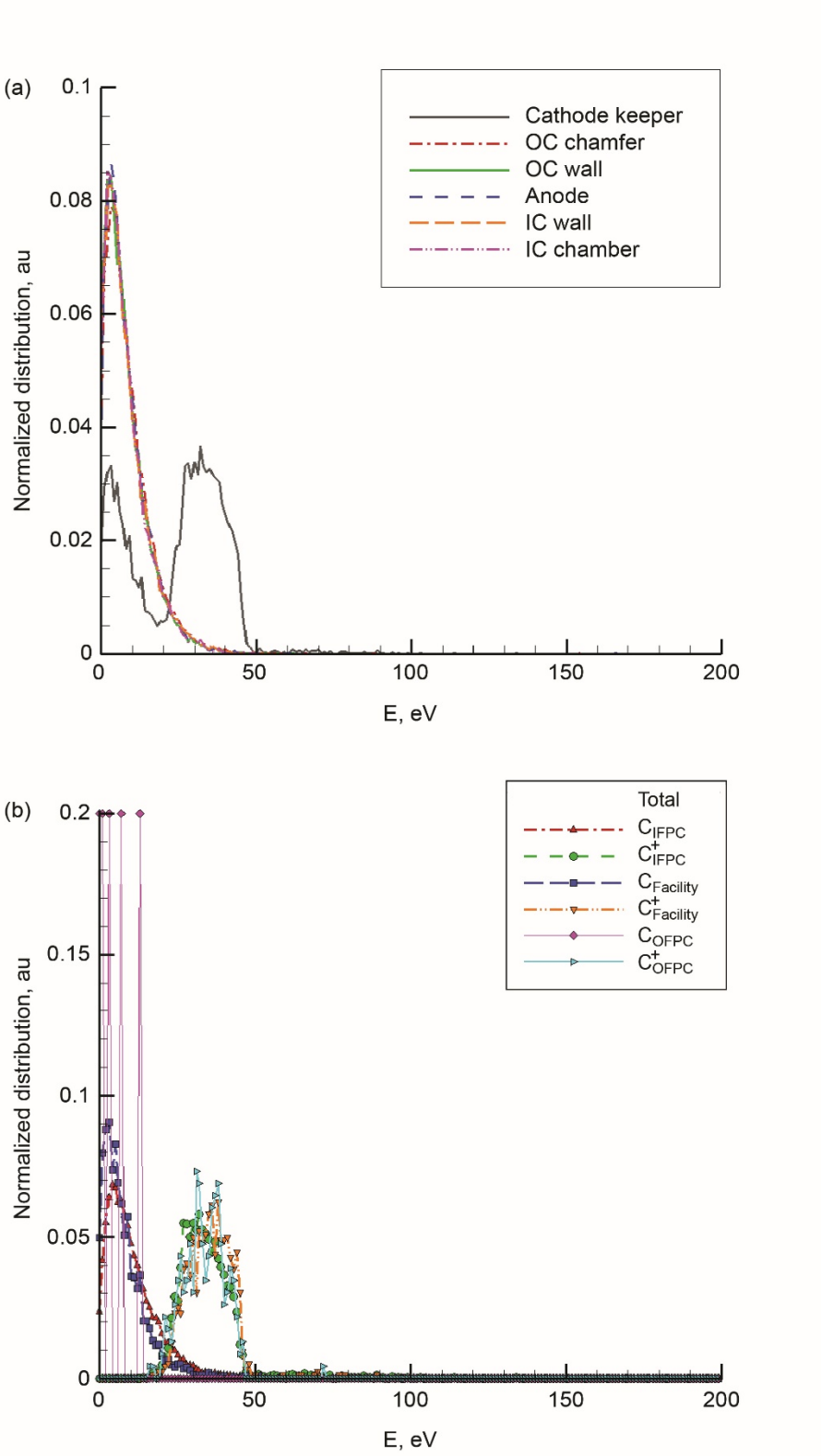

Figure 12.—(a) Energy distributions of backsputtered carbon redepositing on all surfaces. (b) Energy distributions of individual carbon species redepositing on cathode keeper surface. IC, inner channel; IFPC, inner front pole cover; OC, outer channel; OFPC, outer front pole cover.

Conclusions

As a part of the risk-reduction activities for Advanced Electric Propulsion System (AEPS) thruster development, the present study simulated transport of backsputtered carbon from the vacuum facility walls and graphite front pole covers of the thruster. While carbon density is much lower than Xe plasma and neutral densities, the ionization and redeposition were of interest for proper lifetime prediction and contamination modeling purposes. Based on the model used in this study, a few important conclusions were drawn. The redeposition of carbon from the front pole covers on the anode and the main discharge channel wall is mainly dominated by the facility backsputter carbon neutrals, which is up two orders of magnitude higher than the pole cover carbon fluxes. However, the chamfer and front flat parts of the discharge channels have high carbon fluxes from the front pole covers, which is more than an order of magnitude larger than facility carbon flux in some regions. Finally, the cathode keeper collects high fluxes of carbon from both the front pole surfaces and the facility walls. The redeposition rates calculated from the flux of total carbon particles collected at the cathode keeper surface are approximately 0.8 μm/khr. Unfortunately, the net carbon erosion/redeposition rate measurement on the cathode of Technology Demonstration Unit 1 (TDU–1) wear test in Vacuum Facility 5 (VF–5) was too low to be resolved to validate this result.

The energy distributions of carbon neutrals and ions arriving at the anode and discharge channel surfaces preserved their beginning-of-life (BOL) energy distributions, implying that they have undergone no or few collisions. At the cathode keeper surface, the peak energy of carbon ions was found to be around 30 to 40 eV. While there is no sputter yield data on carbon on graphite surfaces, this may not be a concern for keeper erosion because carbon flux is very low compared to Xe.

Future work may include studying the effects of inflow boundary conditions, looking into the effects of molecular carbon species, such as C_2 and C_3, expanding this model and estimating carbon depositions on other important parts of the thruster such as shock isolators, and applying the flux of carbon emanating from pole covers to spacecraft integration model for spacecraft contamination concerns.

References

1. Smith, Bryan K.; Nazario, Margaret L.; and Cunningham, Cameron C.: Solar Electric Propulsion Vehicle Demonstration to Support Future Space Exploration Missions. Space Propulsion 2012, Bordeaux, France, 2012.
2. 115th Congress: National Aeronautics and Space Administration Transition Authorizatin Act of 2017. Public Law 115–10, 2017.
3. NASA Advisory Council: NASA Advisory Council Human Exploration and Operations Committee Meeting Agenda and Minutes. 2017. https://www.NASA.Gov/Sites/Default/Files/Atoms/Files/Nac_Heoc_March_2017_Public_Agenda_Revb.pdf Accessed March 28, 2017.
4. Gerstenmaier, William H.: Progress in Defining the Deep Space Gateway and Transport Plan. NASA Advisory Council Human Exploration and Operations Committee Meeting, 2017. https://www.nasa.gov/sites/default/files/atoms/files/nss_chart_v23.pdf Accessed March 28, 2017.
5. Herman, Daniel A., et al.: Overview of the Development and Mission Application of the Advanced Electric Propulsion System (AEPS). IEPC–2017–284, 2017.
6. Mikellides, Ioannis G., et al.: Magnetic Shielding of the Channel Walls in a Hall Plasma Accelerator. Phys. Plasmas, vol. 18, 2011, p. 033501.
7. Hofer, Richard R., et al.: Design of a Laboratory Hall Thruster with Magnetically Shielded Channel Walls, Phase II: Experiments. AIAA–2012–3788, 2012.
8. Hofer, Richard R., et al.: Wear Test of a Magnetically Shielded Hall Thruster at 3000 Seconds Specific Impulse. IEPC–2013–033, 2013.
9. Goebel Dam, et al.: Pole-Piece Interactions With the Plasma in a Magnetically Shielded Hall Thruster. AIAA 2014–3899, 2014.

10. Williams, George J., et al.: Wear-Testing of the HERMeS Thruster. AIAA 2016–5025, 2016.
11. Sekerak, Michael, et al.: Wear Testing of a Magnetically Shielded Hall Thruster at 2000 s Specific Impulse. IEPC–2015–155, 2015.
12. Williams, George J., et al.: Wear Trends of the HERMeS Thruster as a Function of Throttle Point. IEPC–2017–207, 2017.
13. Kamhawi, H., et al.: Performance and Stability Characterization of the HERMeS Thruster With M26 Boron Nitride Discharge Channel. Presented at the 35th International Electric Propulsion Conference, Atlanta, GA, 2017.
14. Polk, James E., et al.: Front Pole Erosion in the 12.5 kW HERMeS Hall Thruster Over a Range of Operating Conditions. IEPC–2017–409, 2017.
15. Ortega, A.L.; Mikellides, I.G.; and Chaplin, V.: Hall2De Simulations for the Assessment of Pole Erosion in the 12.5 kW Hall Effect Rocket with Magnetic Shielding (HERMeS). Presented at the 35th International Electric Propulsion Conference, Atlanta, GA, 2017.
16. Gilland, J.H., et al.: Back Sputter Modeling for Hall Thruster Testing. Presented at the 52nd AIAA/SAE/ASEE Joint Propulsion Conference, Salt Lake City, UT, 2016.
17. Jorns, B.A., et al.: Mechanisms for Pole Piece Erosion in a 6-kW Magnetically-Shielded Hall Thruster. Presented at the 52nd AIAA/SAE/ASEE Joint Propulsion Conference, Salt Lake City, UT, 2016.
18. Cai, C.: Theoretical and Numerical Studies of Plume Flows in Vacuum Chambers. Ph.D. Dissertation, Univ. of Michigan, 2005.
19. Bird, G.A.: Molecular Gas Dynamics and the Direct Simulation of Gas Flows. Second ed., Oxford Engineering Science Series, Vol. 42, Oxford, New York, NY, 1994.
20. Bird, G.A.: Monte-Carlo Simulation in an Engineering Context. Prog. Astronaut. Aeronaut., vol. 74 1981, pp. 239−255.
21. Younger, S.M.: Electron Impact Ionization Cross Sections and Rates for Highly Ionized Atoms. J. Quant. Spectrosc. Radiat. Transfer, vol. 26, no. 4, 1981, pp. 329–337.
22. Brook, E.; Harrison, M.F.A.; and Smith, A.C.H.: Measurements of the Electron Impact Ionisation Cross Sections of He, C, O and N Atoms. J. Phys. B: At., Mol. Opt. Phys., vol. 11, no. 17, 1978, p. 3115.
23. Sigmund, Peter: Sputtering by Ion Bombardment Theoretical Concepts. Topics in Applied Physics: Sputtering by Particle Bombardment I: Physical Sputtering of Single-Element Solids, R. Behrisch, ed., Vol. 47, Springer, Berlin, Heidelberg, 1981.
24. Oyarzabel, E., et al.: Molybdenum and Carbon Cluster Angular Sputtering Distributions Under Low Energy Xenon Ion Bombardment. AIAA 2005–3525, 2005.
25. Oyarzabal, E., et al.: Carbon Atom and Cluster Sputtering Under Low-Energy Noble Gas Plasma Bombardment. J. Appl. Phys., vol. 104, no. 4, 2008.
26. Williams, John D.; Johnson, Mark L.; and Williams, Desiree D.: Differential Sputtering Behavior of Pyrolytic Graphite and Carbon-Carbon Composite Under Xenon Bombardment. AIAA 2004–3788, 2004.
27. Burt, Jonathan M.; Josyula, Eswar; and Boyd, Iain D.: Novel Cartesian Implementation of the Direct Simulation Monte Carlo Method. J. Thermophys Heat Transfer, vol. 26, no. 2, 2012, pp. 258–270.